APL Electronic Devices ARTICLE pubs.aip.org/aip/aed

Road bump triboelectric generator excited by a small number of actuations for powering Bluetooth communications

Cite as: APL Electron. Devices 1, 016114 (2025); doi: 10.1063/5.0244986
Submitted: 23 October 2024 • Accepted: 14 January 2025 •
Published Online: 12 March 2025

Ahmad Delbani,[1,2] Dimitri Galayko,[3] Malal Kane,[1] and Philippe Basset[2,a)]

AFFILIATIONS

[1] University Gustave Eiffel, EASE/AME, Bouguenais, France
[2] University Gustave Eiffel, CNRS, ESYCOM, F-77454 Marne-la-Vallée, France
[3] Sorbonne Université, CNRS, LIP6, Paris, France

[a)] philippe.basset@esiee.fr

ABSTRACT

The development of smart roads, designed to autonomously transmit sensor data and support advanced vehicle infrastructure, requires innovative, self-sustaining power solutions. This work explores the potential of mechanical energy harvesting from road traffic using a triboelectric nanogenerator (TENG) embedded in a speed bump to power environmental sensors and enable Bluetooth Low Energy (BLE) communication. To this end, we present an optimization framework to maximize the energy conversion in the early stages of transducer operation by tuning the output capacitor (C_{rect}) of the DC rectifier. Through a combination of analytical modeling, SPICE simulations, and experimental validation using a custom test bench, we show that after the first mechanical actuation, tuning C_{rect} to a value close to the minimum value of the TENG capacitance, and choosing the half-wave rather than the full-wave rectifier configuration, can drastically enhance the energy conversion. For the first actuation, half-wave and full-wave are equivalent as long as C_{rect} is minimized and less than the maximum value of the TENG capacitance. Experiments demonstrate the system's ability to successfully power a 1.8 V BLE module for data acquisition and transmission of four embedded sensors. This work shows the feasibility of harvesting sufficient energy from a low-cost triboelectric generator and with a minimal number of mechanical actuations, enabling practical applications such as vehicle counting or environmental monitoring in smart transportation systems.

I. INTRODUCTION

The evolution of roadways in response to technological advances has created an opportunity for the development of intelligent, autonomous infrastructure. These cutting-edge roadways are designed with automation in mind, capable of transmitting sensor data to vehicles and remote base stations. However, a significant challenge remains: providing an autonomous power supply that can be delivered wirelessly, without the need for regular interventions such as battery changes.[1] In this context, two main categories of ambient energy are relevant: solar energy and mechanical energy.[2,3] Solar energy can be harnessed using solar cells, with innovative applications, such as photovoltaic roads. Conversely, there is a substantial supply of mechanical energy present on pavements. In particular, in densely populated metropolitan areas, there is a significant potential for daily wastage of mechanical energy due to traffic density. The goal of this project is to recover and reuse a portion of the wasted energy to power sensors that can, for instance, count vehicles, measure their weight or speed, and thus develop an intelligent transport system or a database for environmental monitoring of civil engineering infrastructures.[4]

A number of research groups and companies have embraced the concept of photovoltaic roads, which use solar cells placed under a semi-transparent layer on top of the road to convert sunlight into electricity. In Ref. 5, Northmore and Tighe proposed a sandwich structure composed of two laminated panes of tempered glass for the transparent layer and thick panes of glass fiber polyester for the electrical and base layers below. In Ref. 6, two different prototypes

are described, one with a top layer in polycarbonate for the transmission of sunlight and another where the solar cells are enclosed between two rubber layers and the top layer is porous to drain and channel the water. In Ref. 7, a photovoltaic floor is designed, where the solar cells are enclosed by two ethylene-vinyl acetate/polyvinyl butyral foils.

An alternative approach is to convert mechanical energy into an electrical signal from the vehicle's load. Piezoelectric materials are capable of generating an electrical charge when pressure is applied to the surface as a vehicle moves over the road:[8] the installation of piezoelectric cymbals with a diameter of 29 mm directly embedded into the asphalt allows each unit to generate up to 16 μW when a truck wheel passes. In Ref. 9, a piezoelectric pavement system based on sealed 30 × 27 cm^2 piezoelectric ceramic disks has been integrated into the pavement structure. In Ref. 10, a column of PZT-5H piezoelectric ceramics has been tested in several pavement materials and various external conditions, including durability testing up to 500 000 cycles. Compared to the integration of transducers directly inside the pavement, an easier way is to implement the mechanical energy harvesting system inside a speed bump.[11] In Ref. 12, a double V-shaped gear mechanism with commercial electromagnetic generators was implemented in a speed bump module and was able to generate 248 mJ under an actuation of 400 N.

For kinetic energy harvesting, beside piezoelectric and electromagnetic transducers, triboelectric energy generators (TENGs) can also be incorporated into the roads or speed bumps. Essentially, a TENG is as a variable capacitor whose electrodes are separated by air, polarized by a triboelectric dielectric material capable of semi-permanently retaining charges upon contact or friction with a conductor or another dielectric material. TENGs are a sub-class of electrostatic kinetic energy harvesters (e-KEHs) combining the triboelectric effect with the electrostatic induction principle.[13] The mechanical excitation-induced processes of separation and contact/rubbing result in an electrostatic force opposing the mechanical separation of the capacitor plates, thus converting mechanical energy into electricity when the transducer's capacitance decreases.[14] Subsequently, a well-designed power management circuit can supply this generated energy to useful electronic loads, while at the same time maintaining the polarization of the TENG to optimize the power conversion process. To date, TENGs have mostly been tested as an additional skin in tires for harvesting energy from vehicles[15,16] or as road sensors.[17–19]

In this work, we propose a low-cost and autonomous system able to sense environmental parameters and transmit them via Bluetooth Low Energy (BLE) communications from a single passing vehicle/pedestrian. The electrical power is obtained from a triboelectric generator embedded in a speed bump. A new analysis is presented with the objective of optimizing the energy converted in the very first mechanical actuations, starting by an unenergized electrical state. This paper also introduces a method for measuring two crucial electrical parameters of a TENG: its dynamic capacitance variation and its equivalent DC voltage source, representing the built-in voltage of the triboelectric layer. This technique provides a straightforward and effective approach to characterize TENGs, allowing for the measurement of macroscopic parameters that govern TENG output power under various mechanical excitations.

In Sec. II, the proposed road electrostatic transducer embedded in a speed bump and based on tribo-electrification is described, modeled, and characterized. In Sec. III, the optimization study is carried out analytically and by SPICE simulations, then experimentally validated. Finally, in Sec. IV, we described the full systems and the experiments of data transmission.

II. DESCRIPTION AND CHARACTERIZATION OF THE SPEED BUMP TRIBOELECTRIC GENERATOR

A. Description of the transducer

A picture of the transducer and a schematic of its side view are shown in Fig. 1. The active part consists of two aluminum electrodes with a surface area of 625 cm^2 and thickness of 2.5 mm, so it can support the size of car tire. The TENG is built to withstand the pressure of a passing vehicle [Fig. 1(a)]. A tribo-electric layer made of a commercially available 52 μm thick PFA sheet, which has an excellent affinity to trap negative charges for a reasonable low cost, is deposited on one of the electrodes. The PFA sheet is stuck on the electrode with conductive double-sided tape. A thick polyurethane foam layer and plastic insulators are placed between the electrodes and the supporting frame to increase the device reliability. Four metallic springs restore the initial separation between the electrodes after actuation, hence realizing a typical conductor-to-dielectric contact-mode TENG,[20] also known as the gap-closing (GC) mode. Even if considered as less efficient, this configuration has been preferred to the free-standing mode with a gap-closing actuation[21] because of its simplicity of fabrication. The PFA layer is charged due to the triboelectric effect during the contact with the mobile electrode in aluminum. The conversion of the mechanical energy into electrical energy occurs during the gap increase between the two electrodes.

B. Electrical lumped-model of the transducer

1. Description of the model

The electrical model of a TENG is represented as a dipole with an ideal variable capacitor in series connected to either an alternative[20] or a DC voltage source.[22] These two models are equivalent, and the choice between AC and DC sources is a matter of convention and preference.

In this work, the TENG is modelized as a gap-closing variable capacitance C_{TENG} in series with a DC source that we refer to as "built-in" or "tribo-electret" voltage V_{TE}[22] [see Fig. 2(b)]. During the contact, the triboelectric effect facilitates the transfer of positive charges to the aluminum, while negative charges are transferred and trapped at the surface of the PFA layer. This results in the layer behaving as an electret. As a result, a current flows between the electrodes due to electrostatic induction. The negative charges are spread very close to the surface of the tribo-electret material, so that we can define a mean value of its surface charge density σ_{TE}. The thickness of the tribo-electret layer is denoted d_{die}, its permittivity ε_{die}, and its surface area S. We assume that the total charge trapped in the PFA is constant and is noted Q_{TE}. X_{max} indicates the maximum air gap with permittivity ε_0. All these variables are summed up in Fig. 2(a).

TENG's variable capacitance $C_{TENG}(t)$ is equivalent to two capacitors in series. The first is a variable capacitor defined by the mobile electrode and a virtual electrode corresponding to the tribo-electric charge layer on top the PFA film. The second is a constant

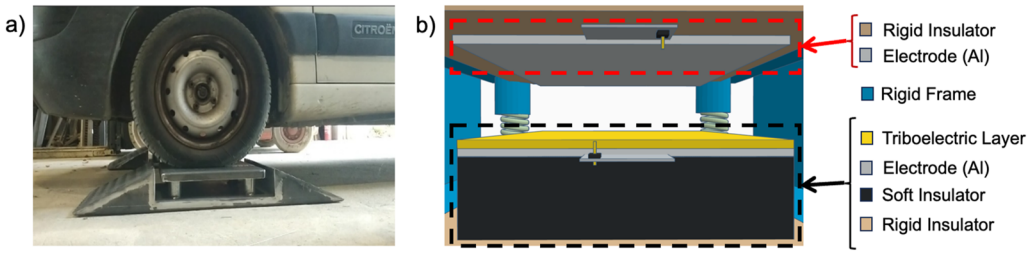

FIG. 1. (a) Road transducer prototype and (b) side view schematic of the transducer.

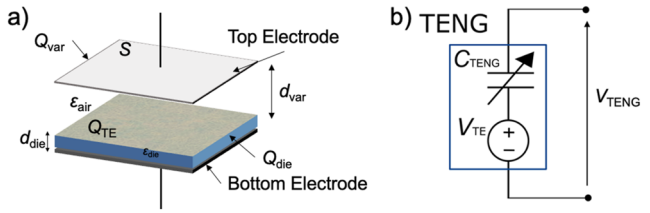

FIG. 2. (a) Schematic of TENG's active layers and (b) its electrical model.

capacitor defined by the aforementioned virtual electrode and the bottom electrode on which the PFA.[22] C_{TENG} varies between C_{Tmax} and C_{Tmin}. C_{Tmax} corresponds to the constant part of C_{TENG}, once the fixed and mobile parts are in contact. C_{Tmin} is defined for the maximum displacement of the mobile electrode X_{max}. Knowing that a planar capacitance C of surface S, with a dielectric of permittivity ε and thickness d, is defined as $C = \varepsilon S/d$, and that two capacitances C_1 and C_2 in series are equivalent to an equivalent capacitance $C_{eq} = C_1C_2/(C_1 + C_2)$, C_{Tmin} and C_{Tmax} are defined as

$$C_{Tmin} = \frac{\varepsilon_0 S}{\frac{d_{die}}{\varepsilon_{die}} + X_{max}}, \tag{1}$$

$$C_{Tmax} = \frac{\varepsilon_0 S}{\frac{d_{die}}{\varepsilon_{die}}}. \tag{2}$$

In case of harmonic displacement, $C_{TENG}(t)$ is given by [assuming $C_{TENG}(0) = C_{Tmin}$]

$$C_{TENG}(t) = \frac{\varepsilon_0 S}{\frac{d_{die}}{\varepsilon_{die}} + \frac{X_{max}}{2} - \frac{X_{max}}{2}\cos(2\pi f t)}. \tag{3}$$

The built-in voltage V_{TE} is defined as[22]

$$V_{TE} = \frac{\sigma_{TE} d_{die}}{\varepsilon_0 \varepsilon_{die}} \tag{4}$$

where V_{TE} corresponds to the tribo-electret layer's average surface voltage.

The zero level of TENG's potential energy regarding the model given in Fig. 2 is defined for the state where the TENG is short-circuited, i.e., $V_{TENG} = 0$. However, it should be noted that in this state, the *internal* energy of the TENG is not zero due to the electrical field created by the charge Q_{TE} in the tribo-electret layer. The potential electric energy of the TENG is defined as for a capacitor,

$$W_{TENG} = \frac{C_{TENG} V_{TENG}^2}{2}.$$

W_{TENG} is equal to the energy that can be recovered from a TENG charged to V_{TENG} voltage by an external load (e.g., by a resistor) connected to the TENG's terminals.

The voltage V_{TE} can be directly measured using an electrometer set above the surface. However, this technique may yield an inaccurate value for V_{TE} due to the non-uniform charge density across the triboelectric layer, which can impact the reliability of the measurement. In addition, it is not a viable option to perform this measurement during the device operation. This built-in polarization is also often indirectly characterized by measuring TENG's open-circuit voltage (V_{OC}) and/or short-circuit current (I_{SC}) during one period of the mechanical forcing,[20] but again with some drawbacks. First, it is challenging to carry out this measurement accurately with standard apparatus given the high amplitude of the dynamic voltage (often several hundred volts) and the low capacitance of TENGs (typically below a few nano-farads). It requires high-voltage measurement apparatus with input impedance in the TΩ range or high-gain current amplifiers.[23] More importantly, V_{OC} and I_{SC} measurements alone cannot discriminate between the effects of electrostatic induction and those of the amount of charge in the triboelectric layer if the dynamics of TENG's variable capacitor is not precisely known. In Sec. II B 3, an indirect measurement technique is used to obtain V_{TE}, which relies on an independent measurement of the variable capacitance dynamics $C_{TENG}(t)$.[24]

2. Transducer's dynamic capacitance measurement

The dynamic capacitance of the TENG is calculated from the phase-shift measurement $\Delta\Phi$ of a RC_{TENG} circuit powered by a high-frequency AC source V_{gen}. From the obtained curve, we can extract the TENG's extremal capacitance ratio $\eta = \frac{C_{Tmax}}{C_{Tmin}}$ under the desired mechanical excitation. The phase-shift $\Delta\Phi$ between V_{gen} (Signal 1) and V_{TENG} (Signal 2) in the $R_\Phi \cdot C_{TENG}(t)$ circuit depicted in Fig. 3(a) is quantified over time to assess $C_{TENG}(t)$. V_{gen} is a sinusoid of constant amplitude with an angular frequency ω significantly higher than the mechanical movement of the TENG electrode(s). Then, $C_{TENG}(t)$ is expressed as[25]

$$C_{TENG}(t) = -\frac{\tan[\Delta\phi(t)]}{R_\Phi \omega}. \tag{5}$$

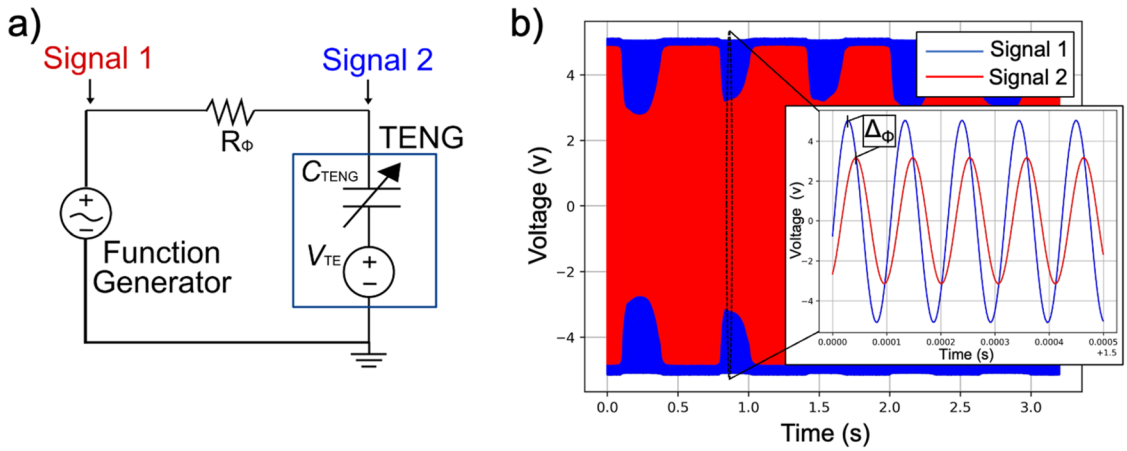

FIG. 3. (a) Circuit for $C_{TENG}(t)$ dynamic measurement based on signals dynamic phase-shift. (b) Signals used for the extraction of $C_{TENG}(t)$.

The sensitivity of $\Delta\Phi$ to the variation of C_{TENG} is maximum at the cutoff frequency of the $R_\Phi C_{TENG}$ network, corresponding to $\Delta\Phi = -\pi/4$. Therefore, the optimal choice of R_Φ, reducing the error propagating from the inaccuracy in phase measurement, is given by

$$R_{\Phi opt} = \frac{1}{C_{TENG}\omega}, \tag{6}$$

where C_{TENG} denotes the expected average value of $C_{TENG}(t)$ (its value can be approached by a first set of measurements using a non-optimal R_Φ).

The TENG capacitance was measured by using this method with $\omega = 2\pi \cdot 9.5$ krad s^{-1} while the road bump is actuated by a walking pedestrian at ~2 Hz. $\Delta\Phi$ is assessed by calculating the time difference between consecutive zero-crossings of both signals (Fig. 3). A preliminary static measurement of C_{Tmax}, with the pedestrian standing on top of the TENG, is obtained with an LCR meter and gives 10 nF, yielding an estimation of 10 kΩ for R_{opt}. Figure 4 illustrates successive dynamic measurements of C_{TENG}, where C_{Tmin} = 420 pF and C_{Tmax} = 6 nF, showing a C_{TENG} ratio η of 14.3 in use.

3. Transducer's build-in triboelectric voltage measurement

The measurement of the built-in voltage V_{TE} is based on observation of the evolution of the half-wave or full-wave rectifiers supplied by the TENG generator (Fig. 5). The saturation voltage across the output capacitance of these stable charge-pumps is related to η and V_{TE} through a simple expression that can be inverted to determine V_{TE}. V_{TE} of either full-wave (FW) or half-wave (HW) rectifier circuit can be calculated from the following formulas:[26]

$$V_{TE} = -V_{sat-FW}\frac{(\eta+1)}{(\eta-1)}, \tag{7}$$

$$V_{TE} = -V_{sat-HW}\frac{1}{(\eta-1)}, \tag{8}$$

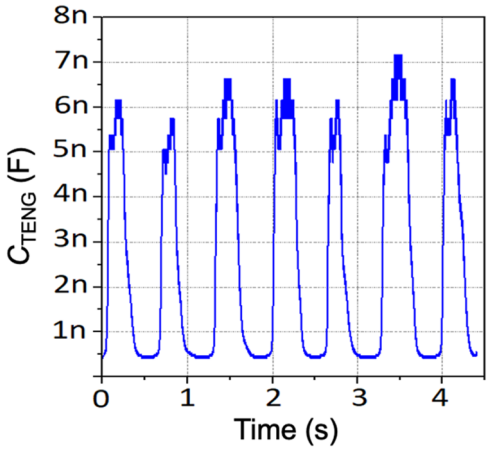

FIG. 4. Road TENG dynamic capacitance value.

where V_{sat-FW} and V_{sat-HW} are the saturation voltages of FW and HW rectifiers, respectively. Given the high capacitance ratio of the transducer, the expected saturation voltage of the rectifiers across C_{rect} is anticipated to exceed 1 kV, making its measurement challenging. To address this, an external parasitic capacitor C_{par} = 4 nF is introduced in parallel with the TENG, reducing its capacitance ratio to η = 2.3 and consequently significantly lowering the saturation voltage.

The output voltage V_{rect} is obtained by measuring the charge Q_{rect} of the output capacitor C_{rect} using a Keithley 6514 electrometer connected in series with C_{rect},

$$V_{rect} = \frac{Q_{rect}}{C_{rect}}. \tag{9}$$

Figure 6 shows the measurements of V_{rect} for both rectifiers across C_{rect} = 10 nF. The saturation voltage of the FW rectifier V_{sat-FW} is 80 V, corresponding to V_{TE} = −207 V. The saturation voltage of the HW rectifier V_{sat-HW} is 260 V, corresponding to

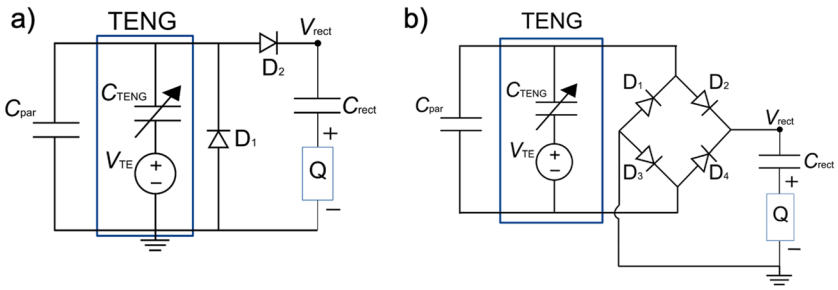

FIG. 5. Circuits for V_{TE} measurements. (a) Half-wave rectifier and (b) full-wave rectifier.

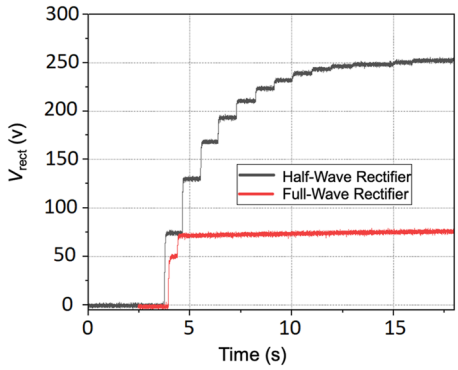

FIG. 6. Output voltage of the HW and FW rectifiers with an external parasitic capacitor of 4 nF to determine the built-in voltage of the tribo-electret material.

$V_{TE} = -206.3$ V. These consistent results by two independent measurement methods validate the TENG model, confirming that this TENG can be modeled by a DC source of $V_{TE} = -206$ V in series with the measured C_{TENG}.

C. Electrical energy generation from the road bump TENG

TENGs can generate very high AC voltage signals at their output, in the range of hundreds to thousands of volts, but with a relatively low current peak of microamps. Most electrical systems need to be powered with a DC voltage, so a rectification is necessary. It can be achieved with stable or unstable charge-pumps. A charge pump rectifies the input AC voltage while generating a dynamic bias (an AC voltage) at the transducer, which is required for energy conversion. A high voltage is also required for a good energy yield. Unstable charge-pumps, such as the Bennet doubler, theoretically have no maximum output DC voltage;[27] they are used when the initial bias voltage of a capacitive transducer is low. In this case, the bias voltage can be increased way beyond the initial bias voltage. On the other hand, stable charge-pumps such as the full-wave (FW) or the half-wave (HW) diode bridge rectifiers experience a saturation, resulting in a DC output voltage of the same order of magnitude as the internal bias voltage of the transducer.[28] Since the internal bias voltage of the TENG is generally very high, stable charge pumps are mainly used with these devices.

In the following experiments, we focus on the HW rectifier, since it will be shown in Sec. III A 3 that it is the best circuit for our practical case. Figure 7(a) shows the output voltage for the first human steps across a value of C_{rect} of 100 nF, which is more than one order of magnitude higher than the maximum value of C_{TENG}. The energy harvested at each step is shown in Fig. 7(b): it increases because the rectifier output voltage is still lower than half its saturation value.[28] However, it is only a few μJ. Considering that the primary purpose of this study is to harvest enough energy from one passing vehicle to power a sensor and send the measurement data to a base station, the harvested electrical energy is insufficient. This illustrates the need to optimize the system to enhance the energy conversion efficiency for a few actuations.

III. OPTIMIZATION FOR A LIMITED NUMBER OF ACTUATIONS

Most of the time, small- or medium-sized mechanical energy harvesters do not collect enough energy to continuously power a system, especially if it includes data transmission. Instead, multiple small amounts of electrical energy are accumulated in a large capacitor over a long period of time. Then, when enough energy is stored in the capacitor, a switch is activated to release a sufficiently large amount of energy for the intended task. This is why the output capacitor C_{rect} of the HW or FW rectifiers is usually one to two orders of magnitude larger than the minimum value of the TENG capacitor. Furthermore, we have shown in previous studies that with stable charge pumps the maximum energy conversion is obtained when the output voltage is equal to half the saturation voltage and that the number of mechanical cycles required to reach this optimum is proportional to C_{rect}/C_{min},[28] which can be a large number. In addition, the maximum average power in conventional unconstrained power maximization settings is an increasing (but saturating) function of C_{rect}, all else equal. However, in our application, only a maximum of 4 actuations (one per wheel) can be obtained for one passing vehicle. Consequently, our optimization problem is quite different than in traditional settings, as we need to maximize the converted energy under a constraint on the number of total actuations at which this energy is evaluated.

A. Description of the method

In the optimization described in Ref. 28, it is assumed that many mechanical cycles are necessary to reach the optimal voltage value. With very few cycles, the previously derived formulas are no longer valid because the optimum output voltage cannot be reached

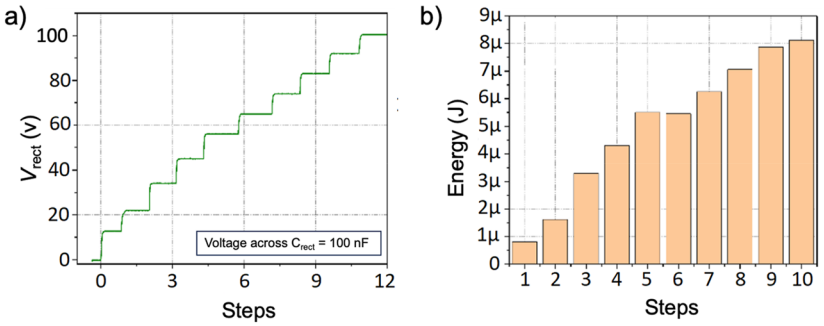

FIG. 7. (a) Voltage across C_{rect} = 100 nF using a half-wave rectifier only and (b) converted energy histogram for each of the first ten mechanical actuations.

under all conditions. In this section, we would like to determine if there is an optimal value for C_{rect} when there are only 1–4 actuation cycles before C_{rect} is discharged to power a system.

1. Equations for the available harvested energy

The system to be optimized is shown in Fig. 8 and consists of a TENG, a stable charge pump as a conditioning circuit (CC), and an ideal switch that discharges its output capacitor C_{rect} into a load each time the switch is operated at C_{Tmin}. It should be noted that such an operation requires a synchronization of the switch with the motion of TENG's mobile electrode. ΔW denotes the electrical energy supplied to the load during the switch actuation. It is calculated as the initial total energy stored in (C_{rect} + C_{TENG}) minus the energy remaining in the two capacitors after the switch actuation,

$$\Delta W = (W_{\mathrm{TENG}_b} + W_{\mathrm{Crect}_b}) - (W_{\mathrm{TENG}_a} + W_{\mathrm{Crect}_a}), \tag{10}$$

where the "b" and "a" indices define the time instants immediately before and after the switch activation and subsequent capacitor discharge, respectively. For analysis, we assume that V_{TE} is constant and C_{rect} is completely and rapidly (relative to the period of mechanical motion) discharged after the switch actuation. Consequently, during the capacitor discharge, C_{TENG} remains at C_{Tmin}. The energy terms in Eq. (10) are then defined as follows:

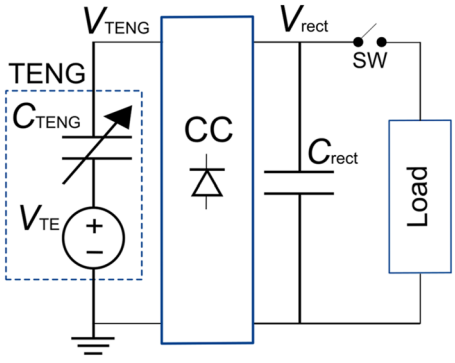

FIG. 8. System used for analysis.

$$\begin{cases} W_{\mathrm{TENG}_b} = \dfrac{C_{\mathrm{Tmin}}}{2} V_{\mathrm{Crect}_0^2}, \\ W_{\mathrm{Crect}_b} = \dfrac{C_{\mathrm{rect}}}{2} V_{\mathrm{Crect}_0^2}, \\ W_{\mathrm{TENG}_a} = W_{\mathrm{Crect}_a} = 0. \end{cases} \tag{11}$$

Expanding Eq. (10) with Eq. (11) leads to

$$\Delta W = \frac{1}{2} V_{\mathrm{rect}_0}^2 C_{\mathrm{Tmin}} (\zeta + 1), \tag{12}$$

where $\zeta = \frac{C_{rect}}{C_{Tmin}}$.

In a stable charge pump, the general law governing V_{rect} throughout C_{TENG}'s variation cycles i is given by

$$V_{\mathrm{rect}_{i+1}} = \alpha V_{\mathrm{rect}_i} + \beta, \tag{13}$$

where α and β are coefficients that depend on the TENG's parameters and the charge-pump architecture, respectively.[28] For the HW rectifier,

$$\begin{cases} \alpha_{\mathrm{HW}} = \dfrac{\zeta}{\zeta + 1}, \\ \beta_{\mathrm{HW}} = -V_{\mathrm{TE}} \dfrac{(\eta - 1)}{\zeta + 1}, \end{cases} \tag{14}$$

where $\eta = \frac{C_{Tmax}}{C_{Tmin}}$.

For the FW rectifier, the evolution of the output voltage depends on the value of the load capacitor C_{rect}. If $C_{rect} < C_{Tmax}$, the operation of the charge pump is degenerated so that the saturation arrives after the first cycle, yielding for all $i > 0$ [Eq. (7)],[28]

$$V_{\mathrm{rect}_i} = -V_{\mathrm{TE}} \frac{\eta - 1}{\eta + 1}.$$

For $C_{rect} > C_{Tmax}$, the evolution is given by (13) with

$$\begin{cases} \alpha_{\mathrm{FW}} = \dfrac{(\zeta - 1)}{(\zeta + 1)} \dfrac{(\zeta - \eta)}{(\zeta + \eta)}, \\ \beta_{\mathrm{FW}} = -V_{\mathrm{TE}} \dfrac{2\zeta}{(\zeta + 1)} \dfrac{(\eta - 1)}{(\zeta + \eta)}. \end{cases} \tag{15}$$

Knowing α and β for a given circuit, the expression of V_{rect} for a specific switch actuation cycle can be injected into the pre-derived expression of ΔW in Eq. (12). Therefore, we get the equation of the available energy with respect to C_{rect}, and we can look for a possible optimum.

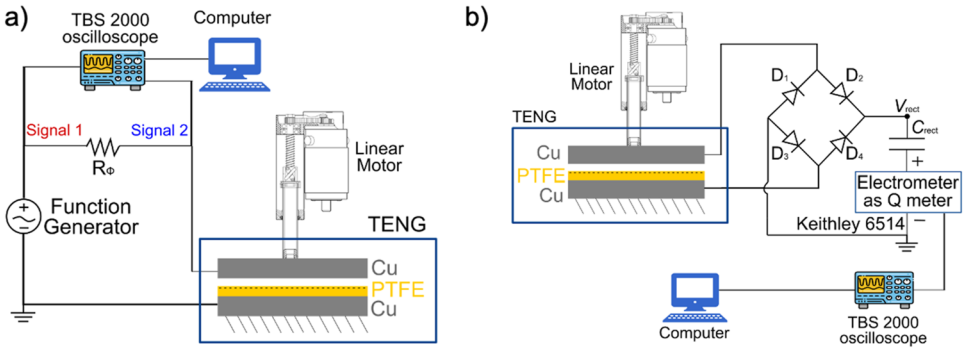

FIG. 9. Schematics of the experimental setups for the TENG characterization. (a) Setup for the dynamic capacitance measurement. (b) Setup for the measurement of V_{TE}.

2. Characterization of the TENG used for validation of the optimization

To evaluate the proposed optimization, experiments are conducted with a simple transducer consisting of two 9 × 9 cm^2 copper electrodes, one of which is covered with a 100 μm thick PTFE film from *Goodfellow*. One electrode is fixed, and a linear motor controls the position of the second one. The same method is applied as in Sec. II B to extract the parameters introduced in the analytical model. A schematic of the experimental setup is shown in Fig. 9. The measurements of the dynamic capacitance using the phase-shift technique and the saturation voltage with a FW rectifier are shown in Fig. 10. We get

$$\begin{cases} \eta = \dfrac{C_{Tmax}}{C_{Tmin}} = \dfrac{417\ pF}{127\ pF} = 3.3, \\ V_{TE} = -V_{sat_{FW}} \dfrac{(\eta+1)}{(\eta-1)} = -188\ V. \end{cases} \tag{16}$$

3. Calculation and SPICE simulation of the available harvested energy

The calculations of the energy available after n = 1, 2, 3, and 4 cycles are performed with a Python scrip, using the recurrent Eq. (13) with the initial value $V_{rect0} = 0$. For each value of n, the value of V_{rect} at the end of the nth cycle is calculated and then Eq. (12) is applied to obtain ΔW for each n. The SPICE simulation, which uses a behavioral model of a variable capacitor and ideal diodes, provides exactly the same results.

Figure 11 shows the curves of the total energy ΔW supplied to the load and the average energy per mechanical cycle as a function of the value of C_{rect} for n = 1–4, for both HW and FW rectifiers. For the HW rectifier [Fig. 11(a)], ΔW displays a maximum for n = 2–4 that increases with the number of cycles, and the optimum value of C_{rect} increases with the number of actuation steps. However, if only one cycle is used, C_{rect} should be minimized. Looking at the average energy per cycle [Fig. 11(b)], it appears that the best configuration is a one-cycle operation when C_{rect} is close to zero.

For the FW rectifier [Fig. 11(c)], the total energy ΔW is the same for any n if $C_{rect} < C_{Tmax}$, since the saturation takes place after the 1st cycle, as mentioned in Sec. III A 1, and it is maximum for the smallest value of C_{rect}. It should be noted that at low C_{rect} in the pF range, ΔW is similar to that of the HW rectifier. For $C_{rect} > C_{Tmax}$, ΔW displays a maximum that increases with n. The optimum C_{rect} for the FW rectifier is one order of magnitude above C_{Tmax}, whereas it is of the same order for the HW rectifier.

B. Experimental validation

Experiments with the HW rectifier are conducted with the TENG presented in Sec. II B, for which C_{Tmin} = 127 pF, C_{Tmax} = 417 pF, and V_{TE} = −188 V. The experimental setup is shown in Fig. 12. The TENG is connected to the rectifier with the electrode covered with PTFE connected to the ground. Each diode of the HW rectifier in Fig. 12(a) corresponds to eight HV diodes connected in series to

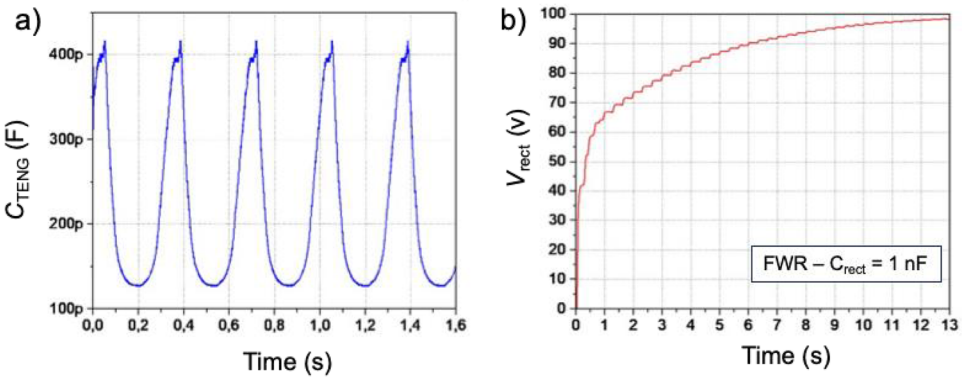

FIG. 10. TENG characterization for optimization study. (a) Dynamic capacitance measurement and (b) full-wave rectifier output.

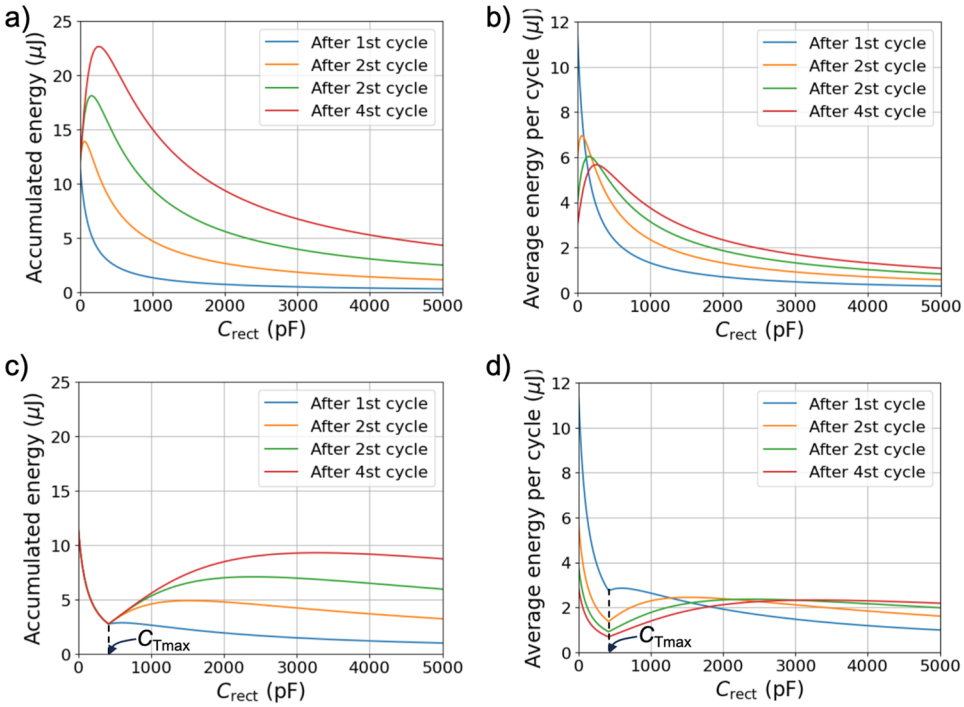

FIG. 11. Harvested energy obtained with SPICE simulations and analytically (identical results) for the first four actuations. (a) Accumulated energy ΔW for the half-wave rectifier, (b) average energy per mechanical cycle for the half-wave rectifier, (c) accumulated energy ΔW for the full wave rectifier, and (d) average energy per mechanical cycle for the full-wave rectifier.

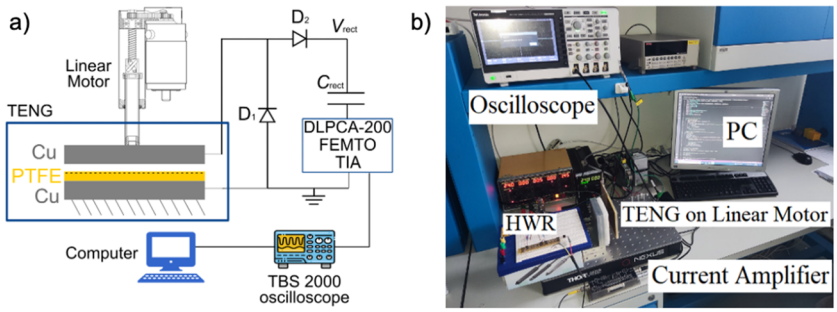

FIG. 12. (a) Schematic and (b) experimental setups for testing the effect of C_{rect} on the available harvested energy.

obtain a reverse breakdown voltage around 1.6 kV. V_{rect} is obtained by measuring the current through C_{rect} with a FEMO DLPCA-200 transimpedance amplifier, which is then integrated and divided by C_{rect}.

Figure 13 shows the calculated available harvested energy from the measurement of V_{rect} for a C_{rect} sweep between 100 pF and 1 nF. As expected, it clearly shows an optimum of C_{rect}, except for a single actuation with the HW rectifier where C_{rect} should be minimized. For those small number of actuations, C_{rect} should have a small value for maximizing the available energy. It can be noted that if higher values of C_{rect} are chosen, the harvested available energy becomes independent with C_{rect}.

IV. DATA TRANSMISSION

A. The power management system (PMS)

Under optimum conditions, the output signal of the TENG speed bump after rectification can reach high values, from 300 to 2 kV. Although this high voltage can improve the level of energy conversion, it must be reduced to 1.8 V for practical use. A solution, to simultaneously maintain a high voltage across the TENG terminals for high energy conversion efficiency and to supply the load with a low voltage, is to implement two-stage power management architecture with an autonomous plasma switch.[29] At each switch actuation, the energy stored in C_{rect} is transferred to a larger capacitor C_{store} through a Buck DC-DC down converter (Fig. 14). The previous optimization study indicates that there exists a value for C_{rect} in the range of the TENG capacitance that minimizes the number of mechanical steps required to reach the switch actuation voltage.

The plasma switch controls the charge transfer between C_{rect} and C_{store}. It is fully autonomous and does not need any additional electronics. It is based on the electrostatic discharge between two metallic wires: at a certain high voltage threshold defined by the gap between both switch electrodes, a current will flow through due the electrical breakdown in a specific gas, here the ambient air.

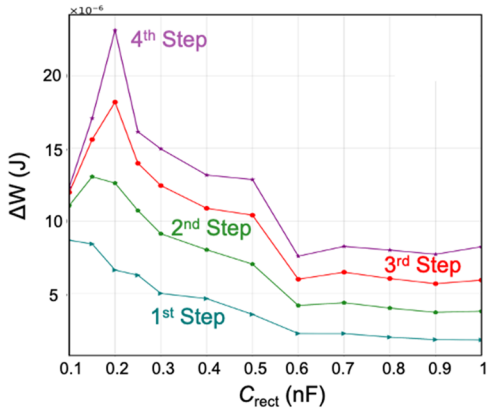

FIG. 13. Experimentally measured harvested energy after different number of first mechanical steps with a HW rectifier.

According to Paschen's law,[30] the breakdown voltage increases as the electrode gap increases, and there is a minimum breakdown voltage around 300 V with a gap of ~5 μm[31] in air. Therefore, the ON-actuation voltage of the switch can be controlled by adjusting the gap properly. If the breakdown voltage can be affected by the environmental changes, fortunately, the fluctuation of breakdown voltage due to humidity change is less than 10%,[32] while the effect of temperature on the breakdown voltage is negligible.[33]

1. Plasma switch characterization

To characterize the plasma switch, we measure the voltage across C_{rect} = 10 nF for several steps with the speed bump TENG shown in Fig. 1 and circuits A + B shown in Fig. 14. The obtained curve is plotted in Fig. 15(a). It shows that the switch has an ON-actuation voltage of around 940 V and OFF-actuation voltage of around 740 V. 120 V are obtained after the first step, corresponding to the generation of 72 μJ. If C_{rect} is decreased to 1 nF, only one step is needed to actuate the plasma switch at 928 V [Fig. 15(b)]. This translates 430 μJ per step: hence, more than 370 μJ has been gained after decreasing the rectification capacitance from 10 to 1 nF.

2. Experiment with the BLE module

This experimental setup consists of the speed bump TENG, the HW rectifier that has been proven by calculation and simulation to be more efficient that the FW rectifier, the plasma switch, a Buck DC–DC down converter, a commercial energy harvesting voltage regulator (LTC-3588), and a BLE module (RIOT-001). The BLE module integrates four low power sensors: temperature, humidity, atmospheric pressure, and luminosity. A dedicated application allows to track on a smartphone the data that are sent continuously. Each diode of the rectifier can withstand up to 3.2 kV. C_{rect}, the output capacitor of the HW rectifier, has a value of 1 nF. The Buck circuit converts the rectifier output from 940 V to less than 10 V

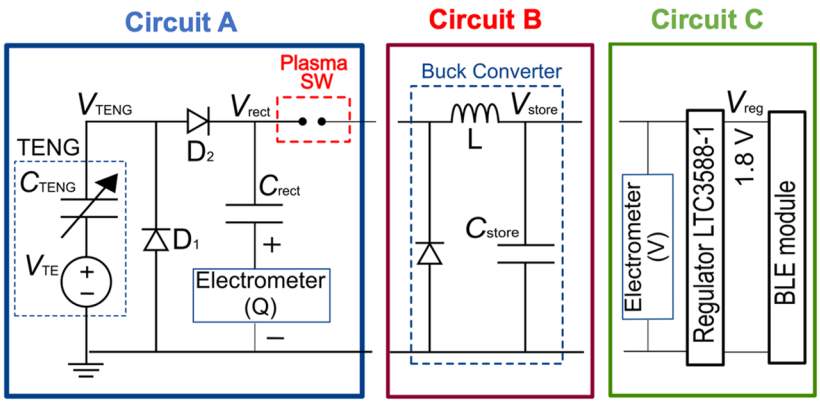

FIG. 14. Full circuit for powering a BLE module and transmit sensors' data.

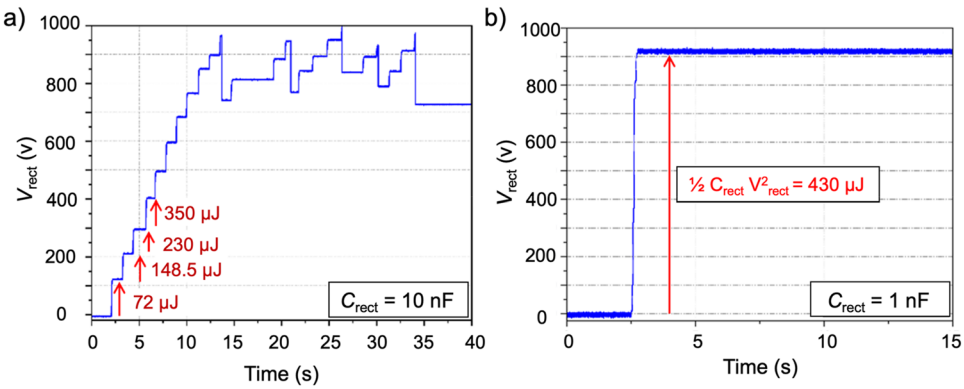

FIG. 15. (a) Voltage across C_{rect} = 10 nF showing the plasma switch hysteresis. (b) Voltage across C_{rect} = 1 nF of a HW rectifier from one mechanical cycle.

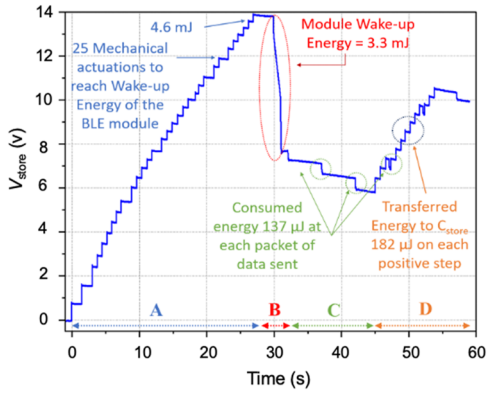

FIG. 16. Voltage evolution across C_{store} during initial charging and transmission with the BLE module.

across C_{store} = 47 μF. At the regulator output, the BLE module is supplied with 1.8 V. Consequently, every time the plasma switch is actuated (with C_{rect} = 1 nF it occurs at every mechanical step), a charge transfer from C_{rect} to C_{store} is achieved.

As shown in Fig. 16, 25 steps are needed to activate the plasma switch from a discharged system, and 3.3 mJ are consumed to wake-up the BLE module. Then, 182 μJ are transferred to C_{store} at each switch actuation (increasing voltage), which triggers the sending of a data packet at the energy cost of around 166 μJ (decreasing voltage). The sensors' data can then be read on an android app.

V. CONCLUSION

In this paper, we have demonstrated that there is an optimal configuration for maximizing the harvested energy in the early stages of a TENG operation by appropriately selecting the value of the DC output rectifier capacitor C_{rect}. Through a combination of analytical studies, simulations, and experimental verification on a dedicated test bench, we found that the available energy can be increased by a factor of three to six by tuning the output capacitor of TENG's rectifier at a low value close to the minimum value of TENG's capacitor. This optimization has been applied to two different energy conditioning circuits, the half-wave and the full-wave rectifiers, and has been carried out for systems where the harvested energy is extracted after the first, second, third, or fourth mechanical actuation step. It was found that for more than one actuation step before extracting the harvested energy, the optimal configuration is with C_{rect} close to the minimum value of the TENG capacitor and the half-wave rectifier outperforms the full-wave rectifier. For a single actuation step, C_{rect} must be minimized and the half-wave and full-wave rectifiers are equivalent as long as C_{rect} is less than the maximum value of the TENG's capacitance. Both SPICE simulations and experimental results confirmed the theoretical analysis.

The optimal configuration requires a DC output voltage of 940 V. A second stage following the rectifier is then required to reduce the output to a few volts in order to power typical electronics devices. It should also be noted that the experiments differ slightly from the theory, as the rectifier output capacitor is not fully discharged after each actuation.

Consequently, we have implemented a two-stage power management system (PMS) including a custom-made plasma switch. This system ensures that a buck DC–DC converter operates autonomously without any additional control electronics. The two-stage PMS enabled the continuous driving of a 1.8 V RIOT-001 BLE module by the triboelectric transducer, with data transmitted on each actuation.

The optimization of C_{rect} maximizes the energy converted from the mechanical domain. Other improvements in overall system efficiency are possible, such as fine-tuning the buck converter's passive components. In particular, increasing the inductance of the Buck converter could improve the charge transfer from the high-voltage to the low-voltage stage. In addition, the wake-up energy requirement of the BLE module remains a challenge, as it far exceeds the energy generated per mechanical actuation of the TENG. A potential solution is to maintain the BLE module in a wakeful state, ensuring that the voltage at the BLE input remains above 1.8 V.

In conclusion, the integration of the TENG, optimized two-stage PMS, and BLE module yields promising results for practical applications of road transducers applications, where the system must sense and transmit data when vehicles or pedestrians pass. Triboelectric generators represent a novel and viable energy harvesting technology that could be deployed on roads at low cost as an alternative to other energy harvesting methods. This work brings us a step closer to commercial applications of triboelectric energy harvesting systems, particularly when combined with a tailored power management circuit.

SUPPLEMENTARY MATERIAL

See the supplementary material for the video of the road TENG in action enabling data transmission from four low-power sensors via Bluetooth.

ACKNOWLEDGMENTS

The authors would like to thank Dr. Armine Karami for his contribution to the development of the analytical model proposed in this paper and on the explanation of the bifurcation observed in the dynamics of the full-wave circuit.

AUTHOR DECLARATIONS

Conflict of Interest

The authors have no conflicts to disclose.

Author Contributions

Ahmad Delbani: Conceptualization (equal); Data curation (equal); Formal analysis (equal); Methodology (equal); Validation (equal); Visualization (equal); Writing – original draft (equal); Writing – review & editing (equal). **Dimitri Galayko**: Data curation (equal); Formal analysis (equal); Supervision (equal); Validation (equal); Writing – review & editing (equal). **Malal Kane**: Funding acquisition (equal); Project administration (equal); Resources (equal); Supervision (equal). **Philippe Basset**: Conceptualization (equal); Supervision (equal); Validation (equal); Visualization (equal); Writing – original draft (equal); Writing – review & editing (equal).

DATA AVAILABILITY

The data that support the findings of this study are available from the corresponding author upon reasonable request.

REFERENCES

[1] R. Fedele *et al.*, "Energy harvesting for IoT road monitoring systems," Instrum. Mes. Metrol. **18**(4), 605–623 (2018).
[2] F. Duarte and A. Ferreira, "Energy harvesting on road pavements: State of the art," Proc. Inst. Civ. Eng.: Energy **169**(2), 79–90 (2016).
[3] A. Dawson *et al.*, "Energy harvesting from pavements," in *Climate Change, Energy, Sustainability and Pavements*, edited by K. Gopalakrishnan *et al.* (Springer, 2014), pp. 481–517.
[4] Y. Pang, T. He, S. Liu, X. Zhu, and C. Lee, "Triboelectric nanogenerator-enabled digital twins in civil engineering infrastructure 4.0: A comprehensive review," Adv. Sci. **11**(20), 2306574 (2024).
[5] A. Northmore and S. Tighe, "Innovative pavement design: Are solar roads feasible," in *2012 Transportation Association of Canada Conference (TAC'12)* (Transportation Association of Canada, Fredericton, NB, 2012), see https://research.usc.edu.au/esploro/outputs/conferencePaper/Innovative-Pavement-Design-Are-Solar-Roads-Feasible/99450374302621.
[6] A. S. Dezfooli *et al.*, "Solar pavement: A new emerging technology," Sol. Energy **149**, 272–284 (2017).
[7] T. Ma *et al.*, "Development of walkable photovoltaic floor tiles used for pavement," Energy Convers. Manage. **183**, 764–771 (2019).
[8] A. Moure *et al.*, "Feasible integration in asphalt of piezoelectric cymbals for vibration energy harvesting," Energy Convers. Manage. **112**, 246–253 (2016).
[9] H. Xiong and L. Wang, "Piezoelectric energy harvester for public roadway: On-site installation and evaluation," Appl. Energy **174**, 101–107 (2016).
[10] Y. Cao, F. Zhang, A. Sha, Z. Liu, J. Li, and Y. Hao, "Energy harvesting performance of a full-pressure piezoelectric transducer applied in pavement structures," Energy Build. **266**, 112143 (2022).
[11] G. del Castillo-García, E. Blanco-Fernandez *et al.*, "Energy harvesting from vehicular traffic over speed bumps: A review," Proc. Inst. Civ. Eng.: Energy **171**(2), 58–69 (2018).
[12] M. Sun, W. Wang, P. Zheng, D. Luo, and Z. Zhang, "A novel road energy harvesting system based on a spatial double V-shaped mechanism for near-zero-energy toll stations on expressways," Sens. Actuators, A **323**, 112648 (2021).
[13] F.-R. Fan, Z.-Q. Tian, and Z. Lin Wang, "Flexible triboelectric generator," Nano Energy **1**(2), 328–334 (2012).
[14] P. Basset, E. Blokhina, and D. Galayko, *Electrostatic Kinetic Energy Harvesting* (John Wiley & Sons, 2016).
[15] Y. Pang *et al.*, "Textile-inspired triboelectric nanogenerator as intelligent pavement energy harvester and self-powered skid resistance sensor," Appl. Energy **348**, 121515 (2023).
[16] W. Seung *et al.*, "Dual friction mode textile-based tire cord triboelectric nanogenerator," Adv. Funct. Mater. **30**, 2002401 (2020).
[17] X. Yang *et al.*, "Triboelectric sensor array for internet of things based smart traffic monitoring and management system," Nano Energy **92**, 106757 (2022).
[18] D. Heo *et al.*, "Triboelectric speed bump as a self-powered automobile warning and velocity sensor," Nano Energy **72**, 104719 (2020).
[19] L. Sarkar, G. Karmakar, S. Ghosh, A. Sett, and T. K. Bhattacharyya, "Triboelectric nanogenerator as next generation traffic monitoring system: Concept and modelling," Nano Energy **121**, 109212 (2024).
[20] S. Niu *et al.*, "Theoretical study of contact-mode triboelectric nanogenerators as an effective power source," Energy Environ. Sci. **6**(12), 3576 (2013).
[21] S. Niu *et al.*, "Theory of freestanding triboelectric-layer-based nanogenerators," Nano Energy **12**, 760–774 (2015).
[22] R. Hinchet *et al.*, "Understanding and modeling of triboelectric-electret nanogenerator," Nano Energy **47**, 401–409 (2018).
[23] J. An, P. Chen, C. Li, F. Li, T. Jiang, and Z. L. Wang, "Methods for correctly characterizing the output performance of nanogenerators," Nano Energy **93**, 106884 (2022).
[24] A. Delbani, A. Karami, D. Galayko, M. Kane, and P. Basset, "Simple technique for the electrical characterization of triboelectric nanogenerators and other kinetic energy harvesters with Electret," in *2023 IEEE 22nd International Conference on Micro and Nanotechnology for Power Generation and Energy Conversion Applications (PowerMEMS)*, Abu Dhabi, United Arab Emirates (IEEE, 2023), p. 139–142.
[25] Y. Lu *et al.*, "A batch-fabricated electret-biased wideband MEMS vibration energy harvester with frequency-up conversion behavior powering a UHF wireless sensor node," J. Micromech. Microeng. **26**(12), 124004 (2016).
[26] A. Ghaffarinejad *et al.*, "A conditioning circuit with exponential enhancement of output energy for triboelectric nanogenerator," Nano Energy **51**, 173–184 (2018).
[27] A. Karami, D. Galayko, and P. Basset, "Series-parallel charge pump conditioning circuits for electrostatic kinetic energy harvesting," IEEE Trans. Circuits Syst. I: Regul. Pap. **64**(1), 227–240 (2017).
[28] H. Zhang, D. Galayko, and P. Basset, "General analysis and optimization of a two-stage power management circuit for electrostatic/triboelectric nanogenerators," Nano Energy **103**, 107816 (2022).
[29] H. Zhang *et al.*, "Employing a MEMS plasma switch for conditioning high-voltage kinetic energy harvesters," Nat. Commun. **11**(1), 3221 (2020).
[30] D. B. Go and D. A. Pohlman, "A mathematical model of the modified Paschen's curve for breakdown in microscale gaps," J. Appl. Phys. **107**(10), 103303 (2010).
[31] T. Ono *et al.*, "Micro-discharge and electric breakdown in a micro-gap," J. Micromech. Microeng. **10**(3), 445 (2000).
[32] K. R. Allen and K. Phillips, "Effect of humidity on the spark breakdown voltage," Nature **183**(4655), 174–175 (1959).
[33] H. Fujita *et al.*, "Breakdown voltages of gaseous N_2 and air from normal to cryogenic temperatures," Cryogenics **18**(4), 195–200 (1978).